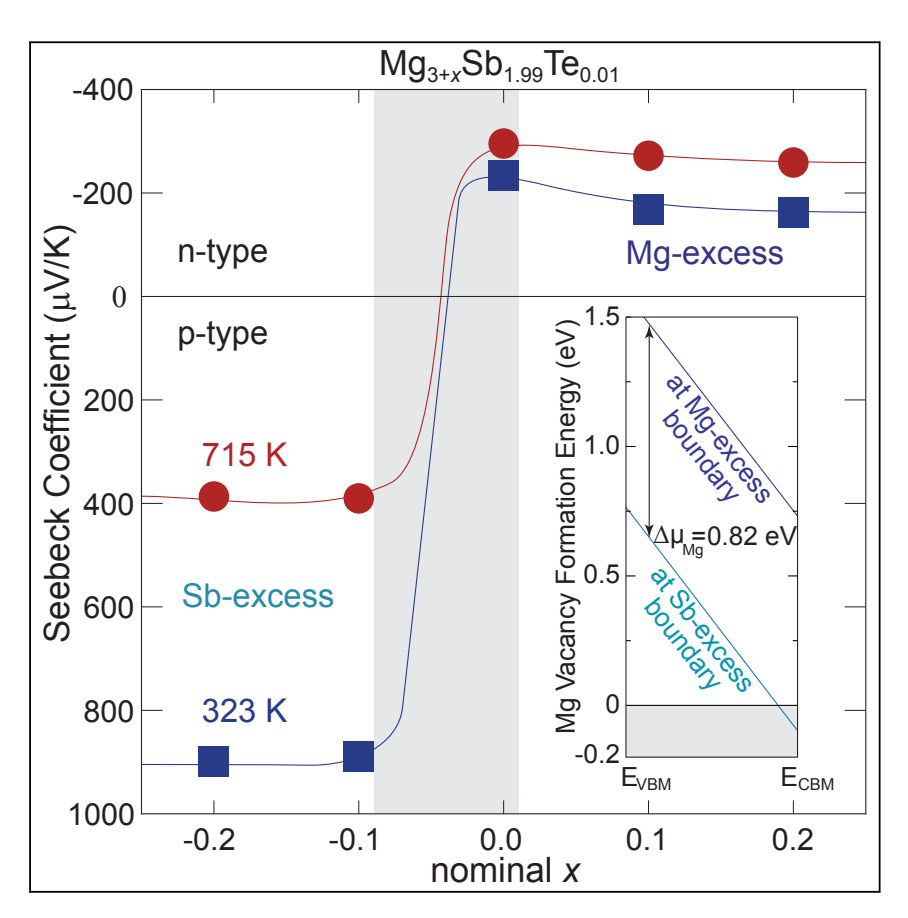


# **Article**

# Phase Boundary Mapping to Obtain *n*-type Mg<sub>3</sub>Sb<sub>2</sub>-Based Thermoelectrics



Despite theoretical predictions of high thermoelectric performance (zT) in n-type Zintl compounds, zT > 1.5 has only been found in Mg<sub>3+x</sub>Sb<sub>1.5</sub>Bi<sub>0.5-y</sub>Te<sub>y</sub> with excess Mg recently. We show here that this has been due to killer Mg-vacancy defects that make Sb-excess material p-type. Recognizing that another thermodynamic state (Mg-excess) exists, we explain the recent discovery and demonstrate zT n-type Mg<sub>3</sub>Sb<sub>2</sub> even without Bi and much less excess Mg. Such phase boundary mapping will enable discovery of new semiconducting states of nominally the same compound.

Saneyuki Ohno, Kazuki Imasato, Shashwat Anand, ..., Eric S. Toberer, Tsutomu Kanno, G. Jeffrey Snyder

pgorai@mines.edu (P.G.) jeff.snyder@northwestern.edu (G.J.S.)

# **HIGHLIGHTS**

Demonstrated high thermoelectric performance (zT) in n-type Mg<sub>3</sub>Sb<sub>2</sub> even without Bi

Determined formation mechanism for n-type  ${\rm Mg_{3+x}Sb_{1.5}Bi_{0.5}}$  to be Mg-vacancy suppression

Proposed phase boundary mapping to fully explore all the thermodynamic states

Ohno et al., Joule 2, 141–154 January 17, 2018 © 2017 Published by Elsevier Inc.

https://doi.org/10.1016/j.joule.2017.11.005





# **Article**

# Phase Boundary Mapping to Obtain *n*-type Mg<sub>3</sub>Sb<sub>2</sub>-Based Thermoelectrics

Saneyuki Ohno,<sup>1,2</sup> Kazuki Imasato,<sup>2</sup> Shashwat Anand,<sup>2</sup> Hiromasa Tamaki,<sup>3</sup> Stephen Dongmin Kang,<sup>1,2</sup> Prashun Gorai,  $^{4,5,*}$  Hiroki K. Sato,  $^3$  Eric S. Toberer,  $^{5,6}$  Tsutomu Kanno,  $^3$  and G. Jeffrey Snyder  $^{1,2,7,*}$ 

# **SUMMARY**

Zintl compounds make excellent thermoelectrics with many opportunities for chemically tuning their electronic and thermal transport properties. However, the majority of Zintl compounds are persistently p-type even though computation predicts superior properties when n-type. Surprisingly, n-type Mg<sub>3</sub>Sb<sub>2</sub>based thermoelectrics have been recently found with exceptionally high figure of merit. Excess Mg is required to make the material n-type, prompting the suspicion that interstitial Mg is responsible. Here we explore the defect chemistry of Mg<sub>3</sub>Sb<sub>2</sub> both theoretically and experimentally to explain why there are two distinct thermodynamic states for Mg<sub>3</sub>Sb<sub>2</sub> (Mg-excess and Sb-excess) and why only one can become n-type. This work emphasizes the importance of exploring all of the multiple thermodynamic states in a nominally single-phase semiconductor. This understanding of the existence of multiple inherently distinct different thermodynamic states of the same nominal compound will vastly multiply the number of new complex semiconductors to be discovered for high zT thermoelectrics or other applications.

# **INTRODUCTION**

Introductory textbooks often wish to tabulate material properties such as electrical and thermal conductivity of pure materials, including semiconductors, such as Si, S, GaAs, and ZnS, thinking of them as "line compounds" where all samples of the same nominal composition will have the same properties. However, it has been known<sup>1,2</sup> from growing binary semiconductors that at least two different AB semiconductors can be produced (at a given temperature) depending on whether the growth is A-excess or B-excess (usually as vapor phase, where vapor pressure adds an additional variable). These two different semiconductors, AB with A-excess (AB equilibrated with A) or AB with B-excess (AB equilibrated with B), have distinctly different properties: one possibly being n-type and the other p-type. In complex systems, especially containing more elements, there are multiple, generally more than two, distinctly defined thermodynamic states.<sup>3</sup> For the discovery of new functional semiconductors, these multiple, distinct states of the same nominal composition expand the space of materials to be investigated. In thermoelectrics, for example, researchers have been examining thousands of nominally single-phase materials for decades in search of, for example, n-type Zintl compounds with predicted high thermoelectric efficiency. 4,5 The discovery of high-performance n-type Mg<sub>3</sub>Sb<sub>2</sub>,6 only recently, highlights the importance of examining all of the distinct thermodynamic states (Mg-excess as well as Sb-excess in this case) by crossing the phase boundaries that are experimentally mapped in nominal composition space, and the fact that perhaps we have been looking at less than half the available new semiconductors that we could have in these past decades.

#### Context & Scale

While there has been good progress in finding high thermoelectric efficiency (zT) ptype Zintl compounds, high zT ntype Zintl compounds have eluded discovery for 10 years despite the theoretical predictions that these would make even better thermoelectric materials. Here we show that even in a "line compound" multiple thermodynamic states exist that profoundly affect the electronic properties by suppressing the formation of unwanted defects differently. To form the desired ntype Mg<sub>3</sub>Sb<sub>2</sub>-based compound it is most critical to make the Mgexcess thermodynamic state. This understanding suggests a synthesis strategy we call "phase boundary mapping" that could be counter-intuitive from the normal perspective that favors thermodynamic phase purity: to add excess constituents until the impurity phase is identified. This strategy can help discover many different versions of any compound, even ones considered to be a "line compound" with no measurable compositional variation.



**Joule** CellPress

#### **Thermoelectric Semiconductors**

Thermoelectric devices can directly convert waste heat into useful electricity, attracting considerable attention as a means to harvest the energy that is currently lost by dissipation. The efficiency of a thermoelectric device is largely dependent on the figure of merit of the thermoelectric materials, which is  $zT = \frac{\alpha^2 \sigma}{\kappa} T$ , where  $\alpha$  is the Seebeck coefficient,  $\sigma$  is the electrical conductivity,  $\kappa$  is the total thermal conductivity, and T is the absolute temperature. Typical zT < 1 values of known materials are insufficient for many proposed applications, making it of interest to explore new materials with beneficial characteristics.

Zintl compounds<sup>9</sup> are a promising class of materials from which good thermoelectrics continue to be discovered. A covalently bonded anionic framework forms the basis of the crystal structure in Zintl compounds,  $^{10,11}$  while the electropositive cations donate electrons satisfying the valence requirement. With anions fulfilling the octet rule with electrons from cations,  $^{12}$  the undoped Zintl compound is, in principle, a semiconductor that can be doped to have an optimum carrier concentration for thermoelectrics. Several Zintl compounds show excellent zT at high temperatures:  $Yb_{14}MnSb_{11}$ ,  $^{13}Ca_9Zn_{4+x}Sb_9$ ,  $^3Sr_3GaSb_3$ ,  $^{14}Ca_5Al_2Sb_6$ ,  $^{15}$  and  $YbCd_2Sb_2$ .  $^{16}$  to name but a few.

Almost all Zintl thermoelectric materials are found to be p-type, while computed electronic structures suggest that some of these persistently p-type materials would also make good, or even better n-type materials because of the band structure. <sup>4,17</sup> For instance, a high-throughput computational search (using density functional theory [DFT] and BoltzTraP) predicted LiZnSb to be an excellent n-type thermoelectric, expected to be more than ten times better than its p-type performance, which reached  $zT \sim 0.1.^{17,18}$  This persistent p-type behavior is also observed in the  $AZn_2Sb_2$  (A = Ca, Yb, Eu, Sr) system (member of the so-called 1-2-2 phases), where the A cation vacancy acts as an "electron killer," preventing n-type samples to form. Studies on this system have revealed how a prudent choice of the A atom could affect the formation energy of the electron killer defects, suggesting that selecting the appropriate A cation is key to overcoming the persistent p-type behavior.

 $Mg_3Sb_2$  is a special case of the 1-2-2 family (Mg occupies both the A and Zn site in  $AZn_2Sb_2$ ) where, after a long history since its first discovery in 1933, <sup>20</sup> the compound has recently been synthesized as *n*-type by Tamaki et al. using excess Mg. <sup>6</sup> This achievement is quite remarkable considering how often this structure type has been considered for thermoelectrics. Previous studies have only found good *p*-type thermoelectrics, starting from  $AZn_2Sb_2$ , <sup>21</sup> and then, including Cd for Zn <sup>16</sup> and Bi for Sb, <sup>22</sup> by which  $zT \sim 1$  has been achieved. Nearly all previous attempts with  $Mg_3Sb_2^{23,24}$  including Mn, Zn, Cd, Na substitution on the Mg site <sup>25–28</sup> and Pb, Bi substitution on the Sb site, <sup>29–33</sup> have produced *p*-type materials. Mn substituted single crystals with largely excess Mg were found to be *n*-type, but with low carrier concentration (<10<sup>18</sup> cm<sup>-3</sup>). <sup>25</sup>

Outstanding n-type Mg<sub>3</sub>Sb<sub>2</sub>-based thermoelectrics had been anticipated based on the conduction band complexity<sup>17</sup> that includes a high-degeneracy Fermi surface with six carrier pockets.<sup>6,34</sup> High valley degeneracy is known to lead to a high thermoelectric material quality factor<sup>35</sup> and is found in most good thermoelectric materials such as Bi<sub>2</sub>Te<sub>3</sub>,<sup>36,37</sup> PbTe,<sup>38,39</sup> Mg<sub>2</sub>(Si,Sn),<sup>40</sup> CoSb<sub>3</sub> skutterudites,<sup>41</sup> and some half-Heusler thermoelectrics.<sup>42</sup>

Tamaki et al. reported n-type Mg<sub>3.2</sub>Sb<sub>1.5</sub>Bi<sub>0.49</sub>Te<sub>0.01</sub> with zT of 1.5 at 715 K followed by similar results by Zhang et al. and Shuai et al.<sup>6,43,44</sup> Figure 1 compares the

<sup>1</sup>Department of Applied Physics and Materials Science, California Institute of Technology, Pasadena, CA 91125, USA

<sup>&</sup>lt;sup>2</sup>Department of Materials Science and Engineering, Northwestern University, Evanston, IL 60208, USA

<sup>&</sup>lt;sup>3</sup>Advanced Research Division, Panasonic Corporation, Soraku-gun, Kyoto 619-0237, Japan

<sup>&</sup>lt;sup>4</sup>Department of Metallurgical and Materials Engineering, Colorado School of Mines, Golden, CO 80401, USA

<sup>&</sup>lt;sup>5</sup>National Renewable Energy Laboratory, Golden, CO 80401, USA

<sup>&</sup>lt;sup>6</sup>Department of Physics, Colorado School of Mines, Golden, CO 80401, USA

<sup>&</sup>lt;sup>7</sup>Lead Contact

<sup>\*</sup>Correspondence: pgorai@mines.edu (P.G.), jeff.snyder@northwestern.edu (G.J.S.) https://doi.org/10.1016/j.joule.2017.11.005

**Joule** Cell<sup>p</sup>ress

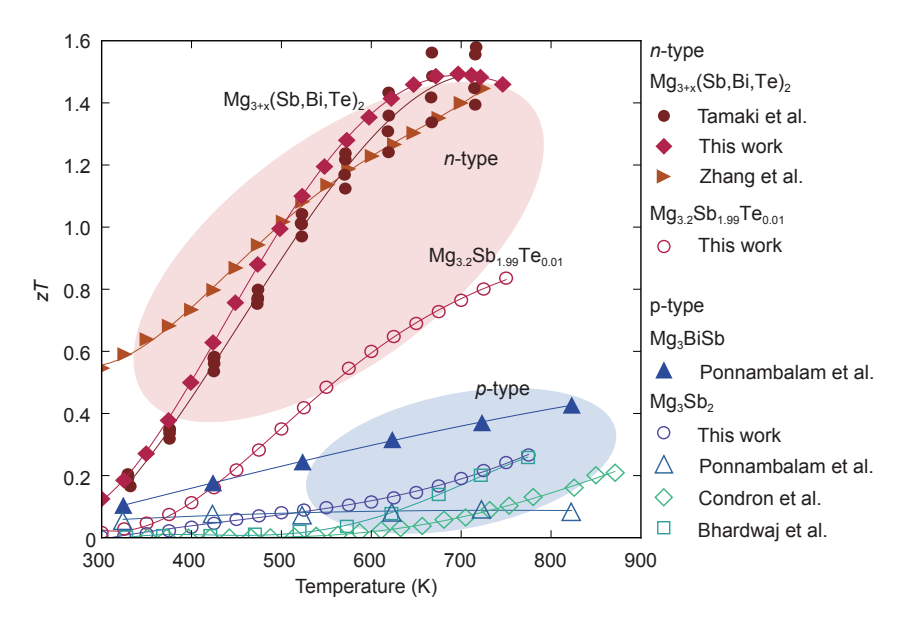


Figure 1. Comparison of zT from n- and p-type  ${\rm Mg_3Sb_2}$ -Based Compounds, Showing the Superior Properties of n-type Materials

The given compositions are nominal compositions. The zT curve from Zhang et al. 43 was scaled using the measured heat capacity rather than the Dulong-Petit value used in the original report.

experimental zT of p- and n-type  $Mg_3Sb_2$ -based compounds including newly synthesized samples that successfully reproduce the optimum n-type composition. A clear contrast in the maximum zT is seen, which is mainly due to the advantage of having a larger valley degeneracy  $(N_v)$  in the conduction band  $(N_v = 6)$  than in the valence band  $(N_v = 1)$  (see Figures S1 and S2).

Due to the substantial excess of Mg in the nominal composition needed  $(Mg_{3.2}(Sb,Bi,Te)_2)$  to make the material n-type, it has been previously proposed that Mg interstitials are responsible for the n-type carriers. Indeed, defect calculations showed that the Mg interstitial defect energy was sufficiently low to enable  $Mg_{3+x}Sb_2$  to become somewhat n-type. Here we find, however, that Mg interstitials are not essential in obtaining n-type  $Mg_3Sb_2$  compounds. In the optimally doped composition, Mg interstitials are eventually so far outnumbered by vacancies that the equilibrium composition is actually Mg deficient, x < 0 in  $Mg_{3+x}(Sb,Bi,Te)_2$ , rather than Mg-excess. This result underscores the significance of the cation vacancies and essential Experimental Procedures to access the thermodynamic state where vacancy formation is most suppressed.

# **RESULTS AND DISCUSSION**

# Defect Chemistry in Mg<sub>3</sub>Sb<sub>2</sub>

In many previous experimental attempts,  $Mg_3Sb_2$  largely remained p-type despite the addition of excess  $Mg.^{24,29}$  Even doping with a substituent that would normally provide n-type carriers has, until recently, not been successful. Such persistent behavior is characteristic of an intrinsic "killer" defect<sup>45</sup> present even in the undoped system that prevents or "pins" the Fermi level ( $E_F$ ) from moving into or near to the conduction band (i.e., limits of concentration of free electrons).

The *p*-type pinning behavior can be readily explained by the presence of a low-energy electron acceptor defect  $V_{\rm Mg}^{2-}$  (Mg<sub>Mg</sub>  $\Rightarrow$   $V_{\rm Mg}^{2-}$  + 2 $h^+$ ) producing excess holes  $h^+$  (or absorbing excess electrons). The formation energy of negatively

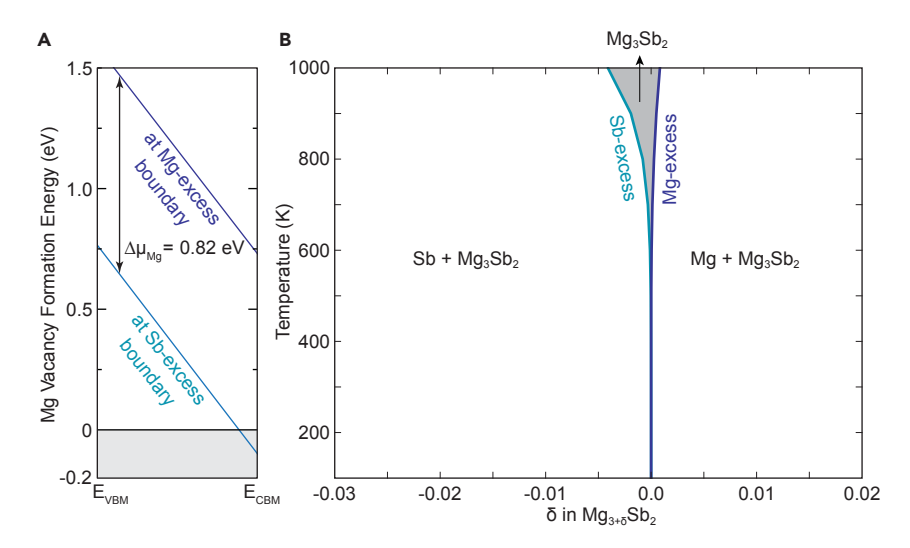


Figure 2. The Mg-Sb Phase Diagram Near  $Mg_3Sb_2$  and Its Influence on the Dominant Defects (A) The Mg-vacancy ( $V_{Mg}^2$ ) formation energy in  $Mg_3Sb_2$  as a function of Fermi level ( $E_F$ ) showing it is a killer acceptor defect for Sb-excess  $Mg_3Sb_2$  (formation energy is negative within the band gap) preventing  $E_F$  from entering conduction band. Mg-excess  $Mg_3Sb_2$  has a high vacancy formation energy even for  $E_F$  inside the conduction band (above  $E_{CRM}$ ).

(B) The calculated Mg-Sb phase diagram near  ${\rm Mg_3Sb_2}$ . The phase boundary on the left (light blue) is the Sb-excess solubility limit determined by the chemical potential of elemental Sb and the boundary on the right side (dark blue) is the Mg-excess limit determined by the chemical potential of elemental Mg.

charged defects such as  $V_{\mathrm{Mg}}^{2-}$  becomes lower with an increasing Fermi level (which indicates having more excess electrons in the system) because it absorbs excess electrons. This makes the slope of the formation energy for  $V_{\rm Mq}^{\ \ 2-}$  versus  $E_F$  in Figure 2A negative (the slope is positive for donor defects). Once a defect formation energy is no longer positive, it will spontaneously form even at T = 0 K. Forming  $V_{\text{Mg}}^{2}$  produces holes and reduces  $E_F$ , enabling the system to reach an equilibrium  $E_F$  and vacancy concentration. Alternatively, if one tries to increase  $E_F$  (by adding impurity donor dopants, for example) to reach the conduction band (i.e., move toward n-type behavior), the formation of Mg vacancies will become more favorable and  $E_F$  will change less than anticipated. If an intrinsic acceptor defect energy reduces to zero by increasing  $E_F$ , then  $E_F$  can never be greater than this value as the intrinsic acceptor defects will always form, reducing the  $E_F$ . In this way intrinsic acceptor defects can pin the  $E_F$  of a material to always be p-type (similarly, intrinsic donor defects can pin the  $E_F$  of a material to always be n-type). For example, in Sb-excess Mg<sub>3</sub>Sb<sub>2</sub>, even when we try to introduce a foreign n-type dopant, the  $E_F$  can never get closer to the conduction band because of the creation of cation vacancies, which move the  $E_F$  back toward the valence band (Figure 2A).

In general, it is reasonable to suspect cation vacancies (Mg vacancies in this case) as the majority defect in Zintl compounds even before resorting to defect energy calculations. Cations generally have much smaller ionic radii than anions, making cation vacancies the likely species for defect formation in antimonides. Although interstitials are also common for small cations such as  ${\rm Mg}^{2+}$ , the persistent p-type behavior observed in  ${\rm Mg}_3{\rm Sb}_2$  suggests that the acceptor Mg vacancies ( ${\rm Mg}_{\rm Mg} \to {\rm V}_{\rm Mg}^{2-} + 2h^+$ ) rather than the electron donor Mg interstitials ( ${\rm Mg}_{\rm Mg} \to {\rm Mg}_{\rm i}^{2+} + 2e^-$ ) explain the behavior. Persistent p-type behavior has been long observed and recently explained in AZn<sub>2</sub>Sb<sub>2</sub> (A = Ca, Yb, Eu, Sr), which has the same crystal structure as

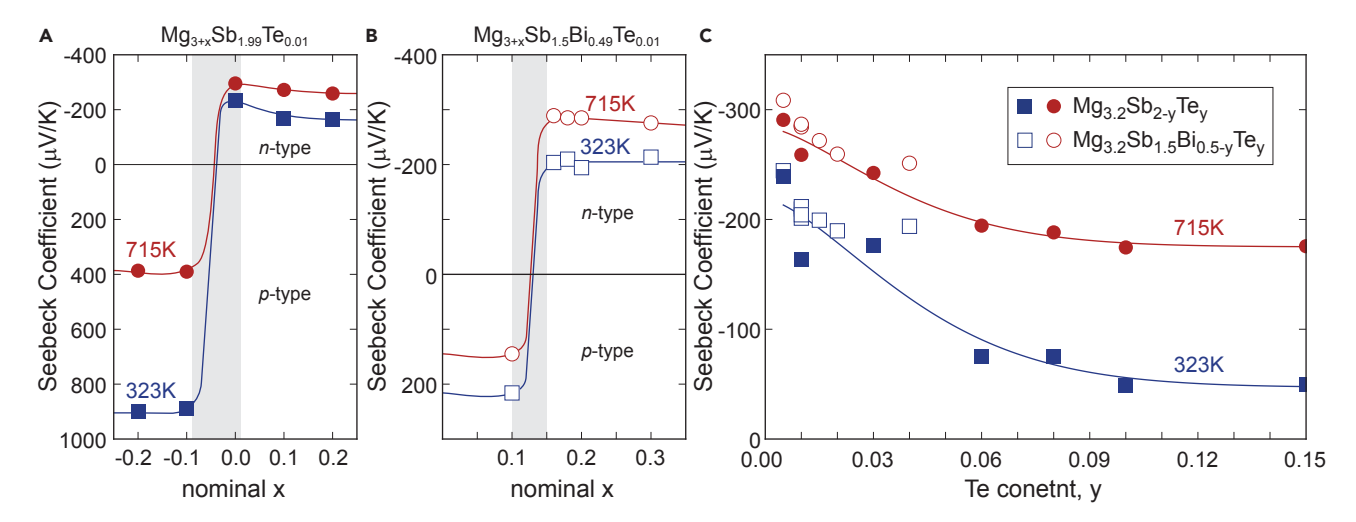


Figure 3. Seebeck Coefficient Dependence on Nominal Composition

(A) The step change of Seebeck coefficient with increasing nominal Mg content in  $Mg_{3+x}Sb_{1.99}Te_{0.01}$  (synthesized using Mg-slug) indicates the abrupt transition in thermodynamic state from Sb-excess to Mg-excess. The thermopower remains almost constant after p-to-n transition even with addition of extra Mg added after  $Mg_3Sb_2$  reaches Mg-excess.

(B) The step change of Seebeck coefficient with increasing nominal Mg content in  $Mg_{3+x}Sb_{1.5}Bi_{0.49}Te_{0.01}$  (synthesized using Mg powder).

(C) The continuous decrease in the thermopower (|S|) up to high Te content for the Mg-excess compositions as expected from an electron donor dopant. Lines are guides to the eye.

 ${
m Mg_3Sb_2}$ . Formation of a sufficient number of stable A-site vacancies actually leads to their suitability as p-type thermoelectric semiconductors without impurity p-type doping. <sup>19,46</sup>

The concentration of intrinsic defects such as  $V_{\rm Mq}^{2-}$  and its temperature dependency can be seen in the equilibrium phase diagram (Figure 2B). Like most valence balanced semiconductors (Zintl compounds), Mg<sub>3</sub>Sb<sub>2</sub> could be described as a line compound because the range of single-phase compositions is very narrow. However, because defects provide entropy, no real compound is exactly a line compound. In Figure 2B the narrow compositional range for Mg<sub>3</sub>Sb<sub>2</sub> is expanded, whereby the significant concentration of the  $V_{\rm Mg}^{2-}$  vacancies is manifested in the extension of the Mg<sub>3</sub>Sb<sub>2</sub> single-phase composition range at the Sb-excess side of the single-phase region. The extension of the phase width at the Mg-excess side is much less due to the higher defect energy of Mg interstitials. For a nominal composition (i.e., overall starting composition) that is Mg-excess (900 K), e.g.,  $Mg_{3.2}Sb_2$ , the actual composition of the matrix phase ( $Mg_3Sb_2$  phase) would be fixed at the Mg-excess side phase boundary yielding an intrinsic composition of  $Mg_{3+\delta}Sb_2$ , where  $\delta$  = 0.0005. We note that the large Mg solubility in  $Mg_3Sb_2$  shown in a previous binary phase diagram (up to Mg<sub>3.28</sub>Sb<sub>2</sub>)<sup>47</sup> is not consistent with our experimental (see Figures S3 and S4; Tables S1 and S2) or computational results (Figure 2B); the original report on which the phase diagram is based showed the Mg-solubility line as uncertain.<sup>48</sup>

These phase boundaries are determined by the chemical potentials of the constituent atoms. The Mg-excess boundary is defined by the Mg-chemical potential in the Mg<sub>3</sub>Sb<sub>2</sub> phase being the same as elemental Mg, while the Sb-excess boundary is defined by the Sb-chemical potential in the Mg<sub>3</sub>Sb<sub>2</sub> phase being the same as elemental Sb. The large chemical potential difference between Mg-excess and Sb-excess in Mg<sub>3</sub>Sb<sub>2</sub>—across a narrow phase width—leads to a nearly step function change in the thermodynamic potentials (manifested in Figure 3). For practical

# **CellPress**

# **Joule**

purposes, this composition range of the  $Mg_3Sb_2$  single-phase region is so narrow that real samples are better thermodynamically defined when their nominal compositions are safely on one side or the other with the desired matrix phase in equilibrium with a small amount (< $\sim$ 2%) of impurity phase; otherwise, the sample is likely to have small but significant compositional variations and result in transport properties indicative of inhomogeneous samples. Therefore, reliable samples of  $Mg_3Sb_2$  should be in one of the two distinct thermodynamic states of accessible samples: Mg-excess and Sb-excess.

The difference in atomic chemical potentials for Mg-excess and Sb-excess Mg<sub>3</sub>Sb<sub>2</sub> (e.g.,  $\Delta \mu_{Mg}$ ) leads to their distinctly different defect formation energies. When the formation of a defect involves the decrease (increase) in the number of atoms, the chemical potential of that atom adds to (subtracts from) the defect formation energy (see Experimental Procedures); the added (subtracted) chemical potential of that atom is identical to that of the other coexisting phase(s) in equilibrium. In Mg-excess Mg<sub>3</sub>Sb<sub>2</sub>, having the Mg-chemical potential of elemental Mg leads to the distinctly higher defect formation energy for  ${V_{\rm Mg}}^{2-}$  (by  $\Delta\mu_{\rm Mg}$  = 0.82 eV) than for  ${V_{\rm Mg}}^{2-}$  in Sb-excess Mg<sub>3</sub>Sb<sub>2</sub> (this difference is thermodynamically guaranteed to exist regardless of the DFT method being used). In this sense, Mg-excess and Sb-excess Mg<sub>3</sub>Sb<sub>2</sub> are thermodynamically different "states." Thus an effective way to suppress the formation of  $V_{Mq}^{2-}$  killer defects is to maintain the Mg<sub>3</sub>Sb<sub>2</sub> in the Mg-excess state. Thermodynamically, it is much more difficult to accommodate Mg vacancies in a system with excess Mg—according to Le Châtelier's principle—and thus a sample nominally Mg-excess would promote filling Mg vacancies. Having a positive formation energy of  $V_{Mq}^{2-}$  at the conduction band edge ( $E_{CBM}$  in Figure 2A) allows Mg-excess Mg<sub>3</sub>Sb<sub>2</sub> to become *n*-type, whereas in Sb-excess Mg<sub>3</sub>Sb<sub>2</sub>, the low and even negative  $V_{\rm Mg}^{2-}$ formation energy near the conduction band will pin the  $E_F$  to p-type. This difference also determines whether an extrinsic (impurity) n-type dopant can actually make Mg<sub>3</sub>Sb<sub>2</sub> n-type, as we explain in the following section.

# Extrinsic Doping with Te Impurities in Mg<sub>3</sub>Sb<sub>2-v</sub>Te<sub>v</sub>

The high concentration ( $\sim 10^{20}$ /cm<sup>3</sup>) of excess electrons needed to make a good thermoelectric is typically supplied by extrinsic, or impurity dopants such as Te atoms (with 6 valence electrons) replacing an Sb (with only 5 valence electrons). These electrons in the conduction band are accounted for by increasing  $E_F$  toward the conduction band edge ( $E_{CBM}$ ).

With Te-doping,  $E_F$  can be moved higher in Mg<sub>3</sub>Sb<sub>2-y</sub>Te<sub>y</sub> but the effect may be almost entirely compensated by the formation of other defects, most notably  $V_{\rm Mg}^{2-}$  killer defects. To calculate these contributing effects (at the typical processing temperature of 900 K) we use standard DFT methods described previously.<sup>6</sup> The important low-energy defects (Figures 4A–4C) that determine  $E_F$  are Mg vacancies on both Mg sites ( $V^{2-}_{\rm Mg(1)}$ ,  $V^{2-}_{\rm Mg(2)}$ ), Te substitution on the Sb site ( $T^{2-}_{\rm Sb}$ ), Mg interstitials (Mg<sup>2+</sup>;), Sb vacancies ( $V^{1+}_{\rm Sb}$ ), and Sb on Mg(1) anti-site defects (Sb<sup>1+</sup><sub>Mg(1)</sub>). For Sb-excess Mg<sub>3</sub>Sb<sub>2-y</sub>Te<sub>y</sub>,  $E_F$  is pinned (Figure 4B), keeping the material p-type up to the solubility limit of Te (0.2 at.% or y  $\approx$  0.01).

The dramatic increase in  $V_{\rm Mg}^{2-}$  defect energy going from Sb-excess to Mg-excess due to the step change in Mg-chemical potential enables a step change in n-type dopability (Figure 4C). Once the vacancies are suppressed, gradually increasing the Te concentration gradually increases the n-type carrier concentration (Figure 3C) and, ultimately, good n-type thermoelectric properties of Mg<sub>3</sub>Sb<sub>2-y</sub>Te<sub>y</sub> with Mg-excess (Figure 1). The predicted n-type carrier concentration (Figure 5) is in

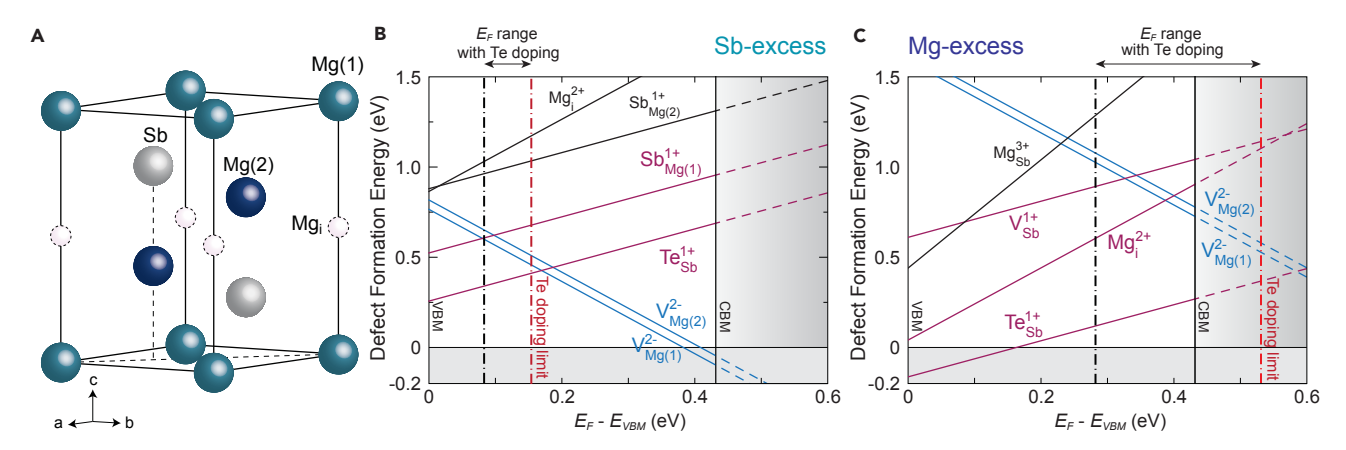


Figure 4. Defect Chemistry in the Te-Doped Mg<sub>3</sub>Sb<sub>2</sub> System

(A) The crystal structure of Mg<sub>3</sub>Sb<sub>2</sub> indicating atomic and interstitial positions.

(B) Defect formation energy  $(\Delta E_{def}^{j})$  for Sb-excess Mg<sub>3</sub>Sb<sub>2</sub> showing the Fermi level at 900 K ( $E_{F}$ ) around the valence band edge even with the addition of Te donor dopants.

(C) Defect formation energy for Mg-excess Mg<sub>3</sub>Sb<sub>2</sub>. The undoped Fermi level ( $E_F$ ) at 900 K (black dash-dotted line) moving deep into the conduction band ( $E_{CBM} < E_F$ ) at the maximum Te-doping limit ( $\approx$ 0.35 at.%) (red dash-dotted line) shows the extrinsic n-type doping capability for Mg-excess Mg<sub>3</sub>Sb<sub>2</sub>. The defect energies were calculated by considering the equilibria of three phases (Mg<sub>3</sub>Sb<sub>2</sub>-Sb-MgTe for B; Mg<sub>3</sub>Sb<sub>2</sub>-Mg-MgTe for C). See also Figure 6A.

good agreement with experimental measurements from Te-doping showing a small reduction in doping effectiveness due to compensating defects.<sup>49</sup>

# Role of Interstitial Mg

The requirement of excess Mg to produce n-type Mg<sub>3</sub>Sb<sub>2</sub> has previously led to the suspicion that Mg<sub>i</sub><sup>2+</sup> interstitials are perhaps responsible. Unlike other 1-2-2 compounds examined previously, Mg<sub>3</sub>Sb<sub>2</sub> could possibly accommodate a small extent of excess of Mg and become slightly n-type; however, at the high n-type doping levels needed for high zT, the concentration of Mg<sub>i</sub><sup>2+</sup> becomes insignificant and less than the concentration of  $V_{\rm Mg}^{2-}$  vacancies as shown in Figure 5.

The ternary Mg-Sb-Te phase diagram (900 K) in the vicinity of the Mg<sub>3</sub>Sb<sub>2</sub> phase (Figures 6B and 6C) illustrates this point. The red dashed line in Figure 6 delineates the compositions when acceptor and donor defects exactly charge-balance, separating compositions that give n- and p-type behavior. The orange dashed line delineates the stoichiometric composition ( $\delta$  = 0) in Mg<sub>3+ $\delta$ </sub>Sb<sub>2-y</sub>Te<sub>y</sub>, separating  $\delta$  < 0 compositions from  $\delta$  > 0 compositions. To avoid confusion, here we explicitly distinguish Mg<sub>3+ $\delta$ </sub>Sb<sub>2-y</sub>Te<sub>y</sub>, where  $\delta$  refers to the actual composition of the matrix phase, from Mg<sub>3+x</sub>Sb<sub>2-y</sub>Te<sub>y</sub>, where x is a nominal (i.e., overall starting) composition. The actual composition of Sb-excess Mg<sub>3+ $\delta$ </sub>Sb<sub>2-y</sub>Te<sub>y</sub>, shown as the light-blue line in Figure 6B (Sb-solubility limit), is always  $\delta$  < 0 and always p-type. Mg-excess Mg<sub>3+ $\delta$ </sub>Sb<sub>2-y</sub>Te<sub>y</sub>, shown as the dark-blue line (Mg-solubility limit), is always n-type but crosses from  $\delta$  > 0 to  $\delta$  < 0 as the Te content increases (Figure 6B) because Mg interstitials are outnumbered by Mg vacancies. This  $\delta$  = 0 line crosses the Mg-excess Mg<sub>3</sub>Sb<sub>2</sub> phase boundary, making the optimum composition samples (around 0.2 at.% of Te) always Mg deficient ( $\delta$  < 0).

# Phase Boundary Mapping to Explore All Equilibrium States of New Phases

 $Mg_3Sb_2$  demonstrates the dramatic difference in electronic properties from two types of samples with a matrix phase composition that is essentially the same. Only Mg-excess  $Mg_3Sb_2$ -based compounds can make efficient n-type



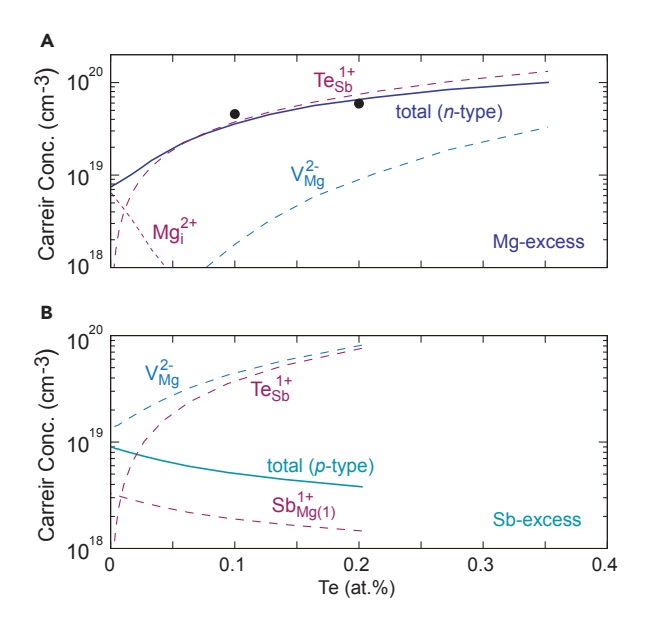


Figure 5. Calculated Net Charge Carrier Concentration (Solid Lines) and the Contributions from Individual Defects (Dashed Lines) in Mg<sub>3</sub>Sb<sub>2</sub> at 900 K with Increasing Te Content

(A) Mg-excess Mg<sub>3</sub>Sb<sub>2</sub>. The *n*-type carrier concentration follows the Te content (Te<sub>Sb</sub><sup>1+</sup>) with some reduction due to Mg vacancies ( $V_{\rm Mg}^{2-}$ ) at the doping concentration needed to make an efficient thermoelectric (0.2 at.% of Te).

(B) Sb-excess Mg<sub>3</sub>Sb<sub>2</sub>. The net carrier concentration is always *p*-type despite the addition of Te donor dopants because of the excessive compensation from Mg vacancies. Data points (black circles) are converted from Hall measurements (see Experimental Procedures) on samples with nominal compositions of Mg<sub>3.2</sub>Sb<sub>2-y</sub>Te<sub>y</sub>, where y = 0.005 and 0.01 in increasing order of Te content.

thermoelectrics. The nominal composition at which the Mg-excess phase boundary is reached turns out to heavily depend on the synthesis route taken. For example, oxidation during preparation or pressing, with oxides in any of the starting elements or even  ${\rm SiO_2}$  or  ${\rm Al_2O_3}$  reaction containers, easily becomes a source of MgO, which effectively removes Mg from the Mg-Sb equilibria. With relatively high vapor pressure and reactivity, Mg loss can also result from vaporization during hot pressing, SPS, or annealing.

Because some Mg loss always exists, the only way to ensure that the Mg-excess phase boundary composition is reached is by detecting Mg impurities in the final material to be measured. Even for reproducible routes of syntheses, there will be a critical nominal composition where the *p*-to-*n* transition happens that may not be at a nominal Mg/Sb ratio of 3:2 and also quite different depending on synthesis conditions (compare the threshold composition within the light-gray regime in Figures 3A and 3B made by Mg powder or slugs). Only by detecting a small amount of elemental Mg or Sb can one be sure which chemical potential defines the properties of the matrix phase.

In general we call this method "phase boundary mapping" in the nominal composition space, whose aim is to purposely make materials in equilibrium with small amounts of impurity phases that exactly define the chemical potentials in order to find the phase boundary in terms of nominal composition.<sup>3</sup> Since most semiconductors are valence balanced (e.g., Zintl compounds<sup>9</sup>), they are typically considered line compounds with narrow phase widths, particularly regarding the cation-to-anion ratio. Therefore, practical samples will generally tend to be on one side or the other, making observation of equilibrium impurity phases the best way to define the

**Joule** Cell<sup>2</sup>ress

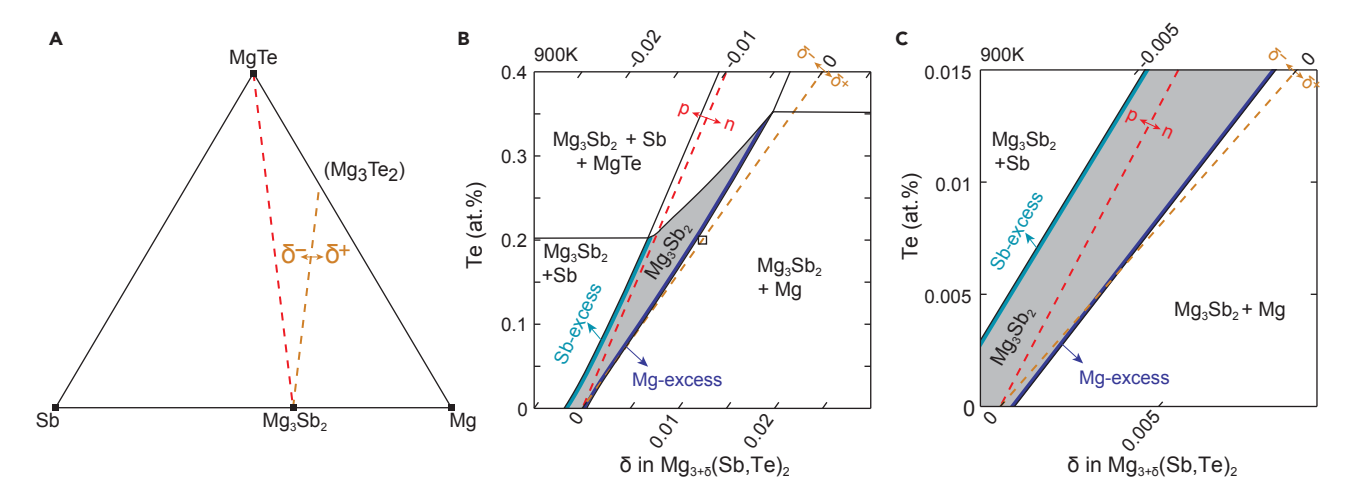


Figure 6. The Ternary Phase Diagram of Mg-Sb-Te

(A) The ternary diagram showing the position of  $\delta$  = 0 in Mg<sub>3+ $\delta$ </sub>(Sb,Te)<sub>2</sub> (orange dashed line) and the line that distinguishes  $\rho$ - and n-type materials in the Mg<sub>3</sub>Sb<sub>2</sub> single-phase region (red dashed line).

(B) Enlarged section of the 900 K ternary phase diagram near the  $Mg_3Sb_2$  single-phase region. The Sb-excess  $Mg_3Sb_2$  phase boundary (light blue) always remains p-type and deficient in Mg ( $\delta < 0$ ) while the Mg-excess  $Mg_3Sb_2$  phase boundary (dark blue) is n-type even though it also is deficient in Mg ( $\delta < 0$ ) when sufficiently doped to make a good thermoelectric (0.2 at.% of Te). The open square on the  $\delta = 0$  line denotes the composition  $Mg_3Sb_{1.99}Te_{0.01}$  (0.2 at.% of Te).

(C) Further enlargement in the vicinity of the phase boundaries.

thermodynamic state. Compound semiconductors will have at least two (most likely more than two) distinct thermodynamic states with distinctly different dopability and transport properties. To explore all synthetically accessible thermodynamic states of the same new semiconductor, one should map all the thermodynamic phase boundaries and continue to change composition (as we added Mg in Mg<sub>3</sub>Sb<sub>2</sub>) until the equilibrium impurity phase changes (as excess Mg was observed instead of Sb). When vacancies are the dominant defects, excess metal should promote *n*-type dopability while excess non-metal should promote *p*-type dopability. Here, we re-emphasize that the main purpose of conducting phase boundary mapping is to fully explore different thermodynamic states in an apparent line compound by crossing the phase boundary, and not to obtain the exact location or actual composition of phase boundaries. The difference in the actual composition between two different thermodynamic states is often not detectable with standard chemical analyses.

A systematic implementation of the phase boundary mapping procedure will lead to a better understanding of the doping capability of new semiconductors for a variety of applications. In thermoelectrics, related approaches have been used to ascertain that cation vacancies are killer defects that lead to persistent *p*-type materials in Ca<sub>9</sub>Zn<sub>4+x</sub>Sb<sub>9</sub>, <sup>3</sup> YCuTe<sub>2</sub>, <sup>50</sup> Cu<sub>2</sub>Se, <sup>51</sup> ZnSb, <sup>52</sup> Zn<sub>4</sub>Sb<sub>3</sub>, <sup>53</sup> and YbZn<sub>2</sub>Sb<sub>2</sub>. <sup>46</sup> We find, in general, several recent cases where significant findings result from a systematic investigation of the phase boundaries: filling capabilities in Skutterudites <sup>54–56</sup> and finding low-defect photovoltaic compounds. <sup>57–59</sup> All these cases highlight the general significance of phase boundary mapping.

# **EXPERIMENTAL PROCEDURES**

# Synthesis

Magnesium slugs (99.95%, Alfa Aesar), antimony shots (99.999%, Alfa Aesar), bismuth granules (99.997%, Alfa Aesar), and tellurium lumps (99.999%, Alfa Aesar) were used for the sample set #1 (see below) as starting elements. Note that the purities reported by the supplier are "metals basis," meaning that the oxygen content is

**Cell**Press

# **Joule**

unknown. Each of the raw materials was cut into small pieces, weighed to be the stoichiometric amount, and loaded into a stainless-steel vial with half-inch stainless-steel balls under argon. Mechanical alloying was conducted by a high-energy mill (SPEX 8000D) for 2 hr. The black powder was extracted from the vial and transferred to a high-density graphite die in the glove box. Subsequently, induction heating rapid hot press (RHP) was conducted at 873 K with 45 MPa for 1 hr with flowing argon. <sup>60</sup> Both geometric and wet densities of the pressed disk-shaped pellets were measured and confirmed to be >95%. Samples of sample set #2 (see below) were prepared with a different method and discussed in Tamaki et al. <sup>6</sup> Following the ball mill by planetary mill with a process control agent (stearic acid), the press was done by SPS instead of RHP.

# Sample Set #1

 ${\rm Mg_{3+x}Sb_2}$  ( $x=-0.1,\,0,\,0.2,\,0.3$ ),  ${\rm Mg_{3+x}Sb_{1.99}Te_{0.01}}$  ( $x=-0.2,\,-0.1,\,0,\,0.1$ , and 0.2),  ${\rm Mg_{3+2}Sb_{2-y}Te_y}$  ( $y=0.005,\,0.01,\,0.03,\,0.06,\,0.08,\,0.1$ , and 0.15), and  ${\rm Mg_{3+x}Sb_{1.5}Bi_{0.49}Te_{0.01}}$  (x=0.03) were prepared and measured at Northwestern University.

# Sample Set #2

 $Mg_{3+x}Sb_{1.5}Bi_{0.49}Te_{0.01}$  (x = 0.1, 0.16, 0.18, 0.2, and 0.3) and  $Mg_{3.2}Sb_{1.5}Bi_{0.49-y}Te_y$  (y = 0, 0.005, 0.01, 0.015, 0.02, and 0.04) were synthesized and measured at Panasonic.

### Characterization

Here we describe the details of characterization for sample set #1 (methods for sample set #2 can be found in Tamaki et al.<sup>6</sup>). Seebeck coefficient was measured with Chromel-Nb thermocouples by oscillating the temperature gradient across the sample under vacuum.<sup>61</sup> The Van der Pauw technique was used to measure electrical resistivity and Hall coefficients with a 2-T magnetic field using pressed Mo probes under dynamic vacuum. The Hall factor used to convert the Hall carrier concentration to a chemical carrier concentration was calculated by using the E<sub>F</sub> estimated from measured thermopower under the assumption of single effective mass model with acoustic phonon scattering. The thermal conductivity was calculated from thermal diffusivity measured by a Netzsch LFA 457 under argon, together with heat capacity. Here the averages of experimental heat capacities (see Bhardwaj and Misra<sup>31</sup> for  $Mg_{3.2}Sb_{1.99}Te_{0.01}$  and Tamaki et al.<sup>6</sup> for  $Mg_{3.2}Sb_{1.5}Bi_{0.49}Te_{0.01}$ ) were applied for a better comparison. The samples were examined by X-ray diffraction performed on polished bulk polycrystalline samples using CuKα radiation, followed by scanning electron microscopy with a Hitachi S-3400N-II. The chemical compositions of Mg<sub>2.9</sub>Sb<sub>2</sub> and Mg<sub>3.2</sub>Sb<sub>2</sub> samples were determined by energy-dispersive X-ray spectroscopy and wavelength-dispersive X-ray spectroscopy. High-resolution synchrotron powder diffraction data of  $Mg_{3+x}Sb_2$  (x = 0.2 and - 0.1) samples were collected using beamline 11-BM at Advanced Photon Source, Argonne National Laboratory, with a wavelength of 0.414537 Å.

# **Phase Diagram Calculation**

The temperature-dependent dilute-limit solvus boundaries for  $Mg_3Sb_2$  in the Mg-Sb-Te ternary phase space were constructed using defect formation energies calculated from first-principles DFT calculations in conjunction with a statistical mechanics model. The DFT calculations were performed within the generalized gradient approximation of Perdew-Burke-Ernzerhof. The projector augmented wave formalism was utilized as implemented in the VASP software package. Defect formation energies were calculated using the standard supercell

Joule Cell<sup>2</sup>ress

approach. <sup>64</sup> A plane-wave cutoff energy of 340 eV along with a 4 × 4 × 4  $\Gamma$ -centered Monkhorst pack k-point grid was used to calculate the total energies of defect supercells containing 90 atoms. The formation energy  $\Delta E_{\rm def}^j$  for defect j was calculated as a function of Fermi level measured from  $E_{\rm VBM}$  ( $\varepsilon_F = E_F - E_{\rm VBM}$ ) and atomic chemical potential due to a set of N-phase equilibrium ( $\mu_i^o + \Delta \mu_i$ ) using

$$\Delta E_{def}^{j}(\{\Delta\mu\},\ \varepsilon_F) = E^{j} - E^{\circ} - \sum\nolimits_{i=1}^{3} \Delta N_{i}^{j}(\mu_{i}^{\circ} + \Delta\mu_{i}) + q^{j}(E_{VBM} + \varepsilon_F) + E_{corr}, \quad \text{(Equation 1)}$$

where  $E^{i}$  and  $E^{o}$  are the DFT total energy of the defect containing Mg<sub>3</sub>Sb<sub>2</sub> supercell and the pristine Mg<sub>3</sub>Sb<sub>2</sub> supercell, respectively.  $\Delta N_i^j$  is the number of atoms of the species i added  $(\Delta N_i^j > 0)$  or removed  $(\Delta N_i^j < 0)$  from the pure supercell to construct the defect supercell.  $\mu_i^o$  is the reference chemical potential of the atom species i in the standard elemental condition and  $\Delta \mu_i$  is the deviation from the reference chemical potential  $\mu_i^o$ .  $\Delta \mu_i = 0$  corresponds to *i*-excess conditions. The reference chemical potentials were obtained by fitting to a set of measured formation enthalpies of compounds under standard conditions. This procedure of determining the reference chemical potentials is inspired by the Fitted Elemental Reference Energies. 65 The region of phase stability of a given compound sets the bounds on  $\Delta \mu_i$ .  $q^i$  and  $E_{VBM}$  are the number of electrons added ( $q^i < 0$ ) or removed ( $q^i > 0$ ) from the defect containing supercell (i.e., the charge state of defect j) and the valence band maximum, respectively.  $E^{j}$  and  $E^{o}$  were computed using the procedure discussed in Stevanović et al.  $^{65}$  and Ortiz et al.  $^{66}$  by relaxing the defect supercells.  $E_{\rm corr}$  is the various finite-size and band-gap corrections that were applied within the supercell approach as outlined in Ortiz et al. 66 and Martinez et al. 67 The underestimation of the band gap in DFT-GGA was rectified by applying band edge shifts determined from GW quasi-particle energy calculations.<sup>64</sup> The following sets of corrections  $(E_{corr})$  were applied to the total energies, following the methodology in Lany and Zunger:<sup>64</sup> (1) image-charge correction for charged defects, (2) potential alignment correction, (3) band-filling correction for shallow defects, and (4) band-gap correction for shallow acceptors/donors. The calculation setup and analyses were performed using a software package developed for automation of point defect calculations. 68 Defect formation energies of all vacancies, antisites, interstitials, and substitutional defects were determined in charge states q = -3, -2, -1, 0, 1, 2, 3. Vacancies and antisites derived from all unique Wyckoff positions in the crystal structure were considered in the calculations. The lowest-energy interstitial geometries were determined by performing Voronoi tessellations followed by structural relaxation with DFT, as implemented in the automated software package.<sup>68</sup>

The position of the Fermi level, the corresponding defect, and charge carrier concentrations at a given temperature were calculated self-consistently by establishing charge neutrality. The defect concentrations were calculated using the Boltzmann relation. As  $\mu_i^o$  is a constant, the dependence of  $\Delta E_{def}^j$  on atomic chemical potential in a set of phase equilibria can essentially be captured through  $\Delta \mu_i$ . We determine  $\Delta \mu_i^{3,m}$  for three-phase region m (described by the notation in the superscript) using

$$\Delta H_k = \sum_{i=1}^3 c_{ik} \Delta \mu_i^{3,m},$$
 (Equation 2)

where  $\Delta H_k$  and  $c_{ik}$  are the formation energies of the phase k and the composition of the atomic species i in this phase. The set of  $\{\Delta \mu_i^{2,l}\}$  for a two-phase regions l common to adjacent three-phase regions m and q were calculated as a weighted sum of  $\Delta \mu_i^{3,m}$  and  $\Delta \mu_i^{3,q}$  using

$$\Delta\mu_i^2 = (1 - \lambda)\Delta\mu_i^{3,m} + (\lambda)\Delta\mu_i^{3,q},$$
 (Equation 3)

where  $\lambda$  (0 <  $\lambda$  < 1) is the weighting fraction.

Joule Cell<sup>2</sup>ress

The temperature dependence of  $\varepsilon_F$  in Equation 1 was determined through reduced Fermi level ( $\eta = \varepsilon_F/k_BT$ ) by numerically solving for the charge neutrality condition given by

$$n - p - \sum_{i} \Delta q^{i} n_{j} = 0,$$
 (Equation 4)

where the number of electrons (n) and holes (p) in the system are calculated using the effective band model equations

$$n, p = 4\pi \left(\frac{2m_{c,v}^*, k_B T}{h^2}\right)^{\frac{3}{2}} F_{1/2}(\eta)$$
 (Equation 5)

$$F_n(\eta) = \int_0^\infty \frac{\epsilon^n d\epsilon}{e^{\epsilon - \eta} + 1},$$
 (Equation 6)

where  $m_V^* = 0.409 m_e$  and  $m_C^* = 0.542 m_e$  are the density of states masses for valence band and conduction band, respectively. The sum in Equation 4 is the charge due to point defects in the system where the concentration of the defect j ( $n_j$ ) is calculated using

$$n_j = N_{\text{site}}^j \exp\left(\frac{-\Delta E_{\text{def}}^j}{k_B T}\right),$$
 (Equation 7)

where  $N_{\text{site}}^{j}$  is the site density of defect the j. The change in the number of atoms of species i (per formula unit) relative to the stoichiometric 0 K phase due to equilibrium concentration of defects is given by

$$\Delta N_i(T, \{\Delta \mu\}) = \sum_i \Delta N_i^j n_j.$$
 (Equation 8)

Using Equation 8, temperature dependence of composition for element i at the phase boundary is calculated by

$$x_i(T, \{\Delta\mu\}) = \frac{N_i^{\circ} + \Delta N_i}{\sum_i (N_i^{\circ} + \Delta N_i)}.$$
 (Equation 9)

For constructing the phase boundary around  $Mg_3Sb_2$  single-phase region we consider the most stable charged states across the band-gap of  $Mg_3Sb_2$  such as  $V_{Mg}^{2+}$  (see Bajaj et al.<sup>69</sup>). The slight underestimation of predicted dopant solubility is what is expected from the dilute-limit approximation, which does not take into account defect interactions and change in vibrational entropy.<sup>70</sup>

# SUPPLEMENTAL INFORMATION

Supplemental Information includes four figures and two tables and can be found with this article online at https://doi.org/10.1016/j.joule.2017.11.005.

# **AUTHOR CONTRIBUTIONS**

S.O., S.D.K., and G.J.S. conceived and designed this research project; S.O. and K.I. carried out synthesis and characterizations at Northwestern University; H.T., H.K.S., and T.K. executed experiments at Panasonic; S.O. analyzed all the experimental data; S.A. performed phase diagram calculation; P.G. conducted DFT defect calculations; S.O., S.D.K., S.A., H.T., P.G., E.S.T., and G.J.S. prepared and edited the manuscript.

# **ACKNOWLEDGMENTS**

The authors would like to thank Prof. Vladan Stevanović of Colorado School of Mines for fruitful discussions regarding the defect formation energy calculation. This work was supported by the NASA Science Mission Directorate's Radioisotope Power Systems Thermoelectric Technology Development. This work made use of the IMSERC



and EPIC facilities at Northwestern University, which has received support from the Soft and Hybrid Nanotechnology Experimental (SHyNE) Resource (NSF NNCI-1542205); the MRSEC program (NSF DMR-1121262) at the Materials Research Center; the State of Illinois and International Institute for Nanotechnology (IIN). Use of the Advanced Photon Source at Argonne National Laboratory was supported by the U.S. Department of Energy, Office of Science, Office of Basic Energy Sciences, under Contract no. DE-AC02-06CH11357. P.G. and E.S.T. acknowledge NSF DMREF 1729594. G.J.S. acknowledges NSF DMREF 1729487.

Received: July 19, 2017 Revised: October 4, 2017 Accepted: November 8, 2017 Published: December 1, 2017

#### **REFERENCES**

- 1. Zhang, S.B., and Northrup, J.E. (1991) Chemical potential dependence of defect formation energies in GaAs: application to Ga self-diffusion. Phys. Rev. Lett. 67, 2339-2342.
- 2. Lany, S., and Zunger, A. (2007). Dopability, intrinsic conductivity, and nonstoichiometry of transparent conducting oxides. Phys. Rev. Lett. 98, 045501.
- 3. Ohno, S., Aydemir, U., Amsler, M., Pöhls, J.-H., Chanakian, S., Zevalkink, A., White, M.A., Bux, S.K., Wolverton, C., and Snyder, G.J. (2017). Achieving zT > 1 in inexpensive Zintl phase Ca<sub>9</sub>Zn<sub>4+x</sub>Sb<sub>9</sub> by phase boundary mapping. Adv. Funct. Mater. 27, 1606361.
- 4. Ortiz, B.R., Gorai, P., Krishna, L., Mow, R., Lopez, A., McKinney, R., Stevanović, V., and Toberer, E.S. (2017). Potential for high thermoelectric performance in n-type Zintl compounds: a case study of Ba doped KAISb4. J. Mater. Chem. A 5, 4036–4046.
- 5. Stark, D., and Snyder, G.J. (2002). The synthesis of CaZn<sub>2</sub>Sb<sub>2</sub> and its thermoelectric properties. International Conference on Thermoelectrics, ICT, Proceedings, 2002-January, 181-184.
- 6. Tamaki, H., Sato, H.K., and Kanno, T. (2016). Isotropic conduction network and defect chemistry in Mg<sub>3</sub>+δSb<sub>2</sub>-Based layered Zintl compounds with high thermoelectric performance. Adv. Mater. 28, 10182-10187.
- 7. Bell, L.E. (2008). Cooling, heating, generating power, and recovering waste heat with thermoelectric systems. Science 321, 1457-1461.
- 8. Snyder, G.J., and Toberer, E.S. (2008). Complex thermoelectric materials. Nat. Mater. 7, 105-114.
- 9. Toberer, E.S., May, A.F., and Snyder, G.J. (2010). Zintl chemistry for designing high efficiency thermoelectric materials. Chem. Mater. 22, 624-634.
- 10. Kazem, N., and Kauzlarich, S.M. (2016). Chapter 288. Thermoelectric properties of Zintl antimonides. In Handbook on the Physics and Chemistry of Rare Earths, Volume 50, G.B. Jean-Claude and K.P. Vitalij, eds. (Elsevier), pp. 177–208.
- 11. Kauzlarich, S.M. (1996). Chemistry, Structure, and Bonding of Zintl Phases and lons (Wiley-VCH).

- 12. Schäfer, H., Eisenmann, B., and Müller, W. (1973). Zintl phases: transitions between metallic and ionic bonding. Angew. Chem. Int. Ed. 12, 694-712.
- 13. Grebenkemper, J.H., Hu, Y., Barrett, D., Gogna, P., Huang, C.-K., Bux, S.K., and Kauzlarich, S.M. (2015). High temperature thermoelectric properties of yb<sub>14</sub>mnsb<sub>11</sub> prepared from reaction of mnsb with the elements. Chem. Mater. 27, 5791-5798.
- 14. Zevalkink, A., Zeier, W.G., Pomrehn, G., Schechtel, E., Tremel, W., and Snyder, G.J. (2012). Thermoelectric properties of Sr<sub>3</sub>GaSb<sub>3</sub>—a chain-forming Zintl compound. Energ. Environ. Sci. 5, 9121.
- 15. Zevalkink, A., Swallow, J., Ohno, S., Aydemir, U., Bux, S., and Snyder, G.J. (2014). Thermoelectric properties of the Ca<sub>5</sub>Al<sub>2-x</sub>In<sub>x</sub>Sb<sub>6</sub> solid solution. Dalton Trans. 43, 15872-15878.
- 16. Wang, X.-J., Tang, M.-B., Chen, H.-H., Yang, X.-X., Zhao, J.-T., Burkhardt, U., and Grin, Y (2009). Synthesis and high thermoelectric efficiency of Zintl phase YbCd2-xZnxSb2. Appl. Phys. Lett. 94, 092106.
- 17. Madsen, G.K. (2006). Automated search for new thermoelectric materials: the case of LiZnSb. J. Am. Chem. Soc. 128, 12140-12146.
- Toberer, E.S., May, A.F., Scanlon, C.J., and Snyder, G.J. (2009). Thermoelectric properties of p-type LiZnSb: assessment of ab initio calculations. J. Appl. Phys. 105, 063701.
- 19. Pomrehn, G.S., Zevalkink, A., Zeier, W.G., van de Walle, A., and Snyder, G.J. (2014). Defectcontrolled electronic properties in AZn<sub>2</sub>Sb<sub>2</sub> Zintl phases. Angew. Chem. Int. Ed. 53, 3422-3426.
- 20. Zintl, E., and Husemann, E. (1933). Bindungsart und gitterbau binaerer magnesiumverbindungen. (12. mitteilung ueber metalle und legierungen). Z. Phys. Chem. 21, 138.
- 21. Gascoin, F., Ottensmann, S., Stark, D., Haile, M.S., and Snyder, G. (2005). Zintl phases as thermoelectric materials: tuned transport properties of the compounds Ca<sub>x</sub>Yb<sub>1-x</sub>Zn<sub>2</sub>Sb<sub>2</sub>. Adv. Funct. Mater. 15, 1860-1864.

- 22. Shuai, J., Geng, H., Lan, Y., Zhu, Z., Wang, C., Liu, Z., Bao, J., Chu, C.W., Sui, J., and Ren, Z (2016). Higher thermoelectric performance of Zintl phases (Eu<sub>0.5</sub>Yb<sub>0.5</sub>)<sub>1-x</sub>Ca<sub>x</sub>Mg<sub>2</sub>Bi<sub>2</sub> by band engineering and strain fluctuation. Proc. Natl. Acad. Sci. USA 113, E4125-E4132.
- 23. Kajikawa, T., Kimura, N., Yokoyama, T. (2003). Thermoelectric properties of intermetallic compounds  $Mg_3Bi_2$  and  $Mg_3Sb_2$  for medium temp. Proceedings of the 22nd International Conference on Thermoelectrics 2003, 305.
- 24. Condron, C.L., Kauzlarich, S.M., Gascoin, F., and Snyder, G.J. (2006). Thermoelectric properties and microstructure of Mg<sub>3</sub>Sb<sub>2</sub>. J. Solid State Chem. 179, 2252–2257.
- 25. Kim, S., Kim, C., Hong, Y.-K., Onimaru, T. Suekuni, K., Takabatake, T., and Jung, M.-H. (2014). Thermoelectric properties of Mn-doped Mg-Sb single crystals. J. Mater. Chem. A 2,
- 26. Xin, H.X., Qin, X.Y., Jia, J.H., Song, C.J., Zhang, K.X., and Zhang, J. (2009). Thermoelectric properties of nanocrystalline (Mg<sub>1-x</sub>Zn<sub>x</sub>)<sub>3</sub>Sb<sub>2</sub> isostructural solid solutions fabricated by mechanical alloying. J. Phys. D Appl. Phys. 42, 165403.
- 27. Zhang, K.X., Qin, X.Y., Xin, H.X., Li, H.J., and Zhang, J. (2009). Transport and thermoelectric properties of nanocrystal substitutional semiconductor alloys  $(Mg_{1-x}Cd_x)_3Sb_2$  doped with Ag. J. Alloys Compounds 484, 498-504.
- 28. Bhardwaj, A., Chauhan, N.S., Goel, S., Singh, V., Pulikkotil, J.J., Senguttuvan, T.D., and Misra, D.K. (2016). Tuning the carrier concentration using Zintl chemistry in Mg<sub>3</sub>Sb<sub>2</sub>, and its implications for thermoelectric figure-of-merit. Phys. Chem. Chem. Phys. 18, 6191-6200.
- 29. Ponnambalam, V., and Morelli, D.T. (2013). On the thermoelectric properties of Zintl compounds  $Mg_3Bi_{2-x}Pn_x$  (Pn = P and Sb). J. Electron. Mater. 42, 1307-1312.
- 30. Xin, H.X., and Qin, X.Y. (2006). Electrical and thermoelectric properties of nanocrystal substitutional semiconductor alloys Mg<sub>3</sub>(Bi<sub>x</sub>Sb<sub>1-x</sub>)<sub>2</sub> prepared by mechanical alloying. J. Phys. D Appl. Phys. 39, 5331–5337.
- 31. Bhardwaj, A., and Misra, D.K. (2014). Enhancing thermoelectric properties of a



- p-type  $Mg_3Sb_2$ -based Zintl phase compound by Pb substitution in the anionic framework. RSC Adv. 4, 34552.
- 32. Kim, S.K., Kim, C.M., Hong, Y.-K., Sim, K.I., Kim, J.H., Onimaru, T., Takabatake, T., and Jung, M.H. (2015). Thermoelectric properties of Mg<sub>3</sub>Sb<sub>2-x</sub>Bi<sub>x</sub> single crystals grown by Bridgman method. Mater. Res. Express *2*, 055902.
- Bhardwaj, A., Rajput, A., Shukla, A.K., Pulikkotil, J.J., Srivastava, A.K., Dhar, A., Gupta, G., Auluck, S., Misra, D.K., and Budhani, R.C. (2013). Mg<sub>3</sub>Sb<sub>2</sub>-based Zintl compound: a nontoxic, inexpensive and abundant thermoelectric material for power generation. RSC Adv. 3, 8504.
- 34. Singh, D.J., and Parker, D. (2013). Electronic and transport properties of Zintl phase AeMg<sub>2</sub>Pn<sub>2</sub>, Ae = Ca,Sr,Ba, Pn = As,Sb,Bi in relation to Mg<sub>3</sub>Sb<sub>2</sub>. J. Appl. Phys. 114, 143703.
- Pei, Y., Wang, H., and Snyder, G.J. (2012). Band engineering of thermoelectric materials. Adv. Mater. 24, 6125–6135.
- Jaworski, C.M., Kulbachinskii, V., and Heremans, J.P. (2009). Resonant level formed by tin in Bi<sub>2</sub>Te<sub>3</sub> and the enhancement of roomtemperature thermoelectric power. Phys. Rev. B 80, 233201.
- 37. Kim, H.-S., Heinz, N.A., Gibbs, Z.M., Tang, Y., Kang, S.D., and Snyder, G.J. (2017). High thermoelectric performance in (Bi<sub>0.25</sub>Sb<sub>0.75</sub>)<sub>2</sub>Te<sub>3</sub> due to band convergence and improved by carrier concentration control. Mater. Today 20, 452–459.
- Pei, Y., LaLonde, A., Iwanaga, S., and Snyder, G.J. (2011). High thermoelectric figure of merit in heavy hole dominated PbTe. Energy Environ. Sci. 4, 2085.
- 39. Pei, Y., Shi, X., LaLonde, A., Wang, H., Chen, L., and Snyder, G.J. (2011). Convergence of electronic bands for high performance bulk thermoelectrics. Nature 473, 66–69.
- Liu, W., Tan, X., Yin, K., Liu, H., Tang, X., Shi, J., Zhang, Q., and Uher, C. (2012). Convergence of conduction bands as a means of enhancing thermoelectric performance of *n*-type Mg<sub>2</sub>Si<sub>1-x</sub>Sn<sub>x</sub> solid solutions. Phys. Rev. Lett. *108*, 166601.
- Tang, Y., Gibbs, Z.M., Agapito, L.A., Li, G., Kim, H.-S., Nardelli, M.B., Curtarolo, S., and Snyder, G.J. (2015). Convergence of multi-valley bands as the electronic origin of high thermoelectric performance in CoSb<sub>3</sub> skutterudites. Nat. Mater. 14, 1223–1228.
- 42. Fu, C., Zhu, T., Pei, Y., Xie, H., Wang, H., Snyder, G.J., Liu, Y., Liu, Y., and Zhao, X. (2014). High band degeneracy contributes to high thermoelectric performance in p-type half-Heusler compounds. Adv. Energy Mater. 4, 1400600.
- Zhang, J., Song, L., Pedersen, S.H., Yin, H., Hung, L.T., and Iversen, B.B. (2017). Discovery of high-performance low-cost n-type Mg<sub>3</sub>Sb<sub>2</sub>based thermoelectric materials with multivalley conduction bands. Nat. Commun. 8, 13901.
- 44. Shuai, J., Mao, J., Song, S., Zhu, Q., Sun, J., Wang, Y., He, R., Zhou, J., Chen, G., Singh, D.J.,

- and Ren, Z. (2017). Tuning the carrier scattering mechanism to effectively improve the thermoelectric properties. Energy Environ. Sci. 10, 799–807.
- 45. Zunger, A. (2003). Practical doping principles. Appl. Phys. Lett. 83, 57.
- Zevalkink, A., Zeier, W.G., Cheng, E., Snyder, J., Fleurial, J.-P., and Bux, S. (2014).
   Nonstoichiometry in the Zintl phase Yb<sub>1-a</sub>Zn<sub>2</sub>Sb<sub>2</sub> as a route to thermoelectric optimization. Chem. Mater. 26, 5710–5717.
- Paliwal, M., and Jung, I.-H. (2009). Thermodynamic modeling of the Mg-Bi and Mg-Sb binary systems and short-rangeordering behavior of the liquid solutions. Calphad 33, 744–754.
- Grube, G., and Bornhak, R. (1934). The shape diagram of magnesium-antimony.
   Elektrochemie Angew. Physikalische Chem. 40, 140–142.
- Toberer, E.S., Zevalkink, A., Crisosto, N., and Snyder, G.J. (2010). The Zintl compound Ca<sub>5</sub>Al<sub>2</sub>Sb<sub>6</sub> for low-cost thermoelectric power generation. Adv. Funct. Mater. 20, 4375–4380.
- Aydemir, U., Pöhls, J.-H., Zhu, H., Hautier, G., Bajaj, S., Gibbs, Z.M., Chen, W., Li, G., Ohno, S., Broberg, D., et al. (2016). YCuTe<sub>2</sub>: a member of a new class of thermoelectric materials with CuTe<sub>4</sub>-based layered structure. J. Mater. Chem. A 4, 2461–2472.
- Kang, S.D., Danilkin, S.A., Aydemir, U., Avdeev, M., Studer, A., and Snyder, G.J. (2016). Apparent critical phenomena in the superionic phase transition of Cu<sub>2-x</sub>Se. New J. Phys. 18, 013024.
- Shabaldin, A.A., Prokof'eva, L.V., Snyder, G.J., Konstantinov, P.P., Isachenko, G.N., and Asach, A.V. (2016). The influence of weak tin doping on the thermoelectric properties of zinc antimonide. J. Electron. Mater. 45, 1871–1874.
- Toberer, E.S., Rauwel, P., Gariel, S., Taftø, J., and Snyder, G.J. (2010). Composition and the thermoelectric performance of β-Zn<sub>4</sub>Sb<sub>3</sub>. J. Mater. Chem. 20, 9877–9885.
- 54. Tang, Y., Chen, S.-W., and Snyder, G.J. (2015). Temperature dependent solubility of Yb in Yb-CoSb<sub>3</sub> skutterudite and its effect on preparation, optimization and lifetime of thermoelectrics. J. Materiomics 1, 75–84.
- Tang, Y., Hanus, R., Chen, S.-W., and Snyder, G.J. (2015). Solubility design leading to high figure of merit in low-cost Ce-CoSb<sub>3</sub> skutterudites. Nat. Commun. 6, 7584.
- Tang, Y., Qiu, Y., Xi, L., Shi, X., Zhang, W., Chen, L., Tseng, S.-M., Chen, S.-W., and Snyder, G.J. (2014). Phase diagram of In-Co-Sb system and thermoelectric properties of In-containing skutterudites. Energy Environ. Sci. 7, 812–819.
- Zawadzki, P., Baranowski, L.L., Peng, H., Toberer, E.S., Ginley, D.S., Tumas, W., Zakutayev, A., and Lany, S. (2013). Evaluation of photovoltaic materials within the Cu-Sn-S family. Appl. Phys. Lett. 103, 253902.
- Baranowski, L.L., Zawadzki, P., Lany, S., Toberer, E.S., and Zakutayev, A. (2016). A review of defects and disorder in multinary

- tetrahedrally bonded semiconductors. Semiconductor Sci. Technol. 31, 123004.
- Martinez, A.D., Ortiz, B.R., Johnson, N.E., Baranowski, L.L., Krishna, L., Choi, S., Dippo, P.C., To, B., Norman, A.G., Stradins, P., et al. (2015). Development of ZnSiP<sub>2</sub> for Si-based tandem solar cells. IEEE J. Photovoltaics 5, 17–21.
- LaLonde, A.D., Ikeda, T., and Snyder, G.J. (2011). Rapid consolidation of powdered materials by induction hot pressing. Rev. Sci. Instrum. 82, 025104.
- Iwanaga, S., Toberer, E.S., LaLonde, A., and Snyder, G.J. (2011). A high temperature apparatus for measurement of the Seebeck coefficient. Rev. Sci. Instrum. 82, 063905.
- 62. Perdew, J.P., Burke, K., and Ernzerhof, M. (1996). Generalized gradient approximation made simple. Phys. Rev. Lett. 77, 3865–3868.
- Kresse, G., and Furthmüller, J. (1996). Efficient iterative schemes for ab initio total-energy calculations using a plane-wave basis set. Phys. Rev. B 54, 11169–11186.
- Lany, S., and Zunger, A. (2009). Accurate prediction of defect properties in density functional supercell calculations. Model. Simulation Mater. Sci. Eng. 17, 084002.
- Stevanović, V., Lany, S., Zhang, X., and Zunger, A. (2012). Correcting density functional theory for accurate predictions of compound enthalpies of formation: Fitted elementalphase reference energies. Phys. Rev. B 85, 115104.
- Ortiz, B.R., Gorai, P., Stevanovic, V., and Toberer, E. (2017). Thermoelectric Performance and Defect Chemistry in n-Type Zintl KGaSb<sub>4</sub>. Chem. Mater. 29, 4523–4534.
- 67. Martinez, A.D., Warren, E.L., Gorai, P., Borup, K.A., Kuciauskas, D., Dippo, P.C., Ortiz, B.R., Macaluso, R.T., Nguyen, S.D., Greenaway, A.L., et al. (2016). Solar energy conversion properties and defect physics of ZnSiP<sub>2</sub>. Energy Environ. Sci. 9, 1031–1041.
- 68. Goyal, A., Gorai, P., Peng, H., Lany, S., and Stevanovic, V. (2017). A computational framework for automation of point defect calculations. Comput. Mater. Sci. 130, 1–9.
- Bajaj, S., Wang, H., Doak, J.W., Wolverton, C., and Jeffrey Snyder, G. (2016). Calculation of dopant solubilities and phase diagrams of X-Pb-Se (X = Br, Na) limited to defects with localized charge. J. Mater. Chem. C 4, 1769–1775.
- Ozoliņš, V., and Asta, M. (2001). Large vibrational effects upon calculated phase boundaries in Al-Sc. Phys. Rev. Lett. 86, 448–451.
- Collins, G.S. (2007). Nonstoichiometry in line compounds. J. Mater. Sci. 42, 1915–1919.
- Imasato, K., Kang, S.D., Ohno, S., and Snyder, G.J. (2017). Band engineering in Mg<sub>3</sub>Sb<sub>2</sub> by alloying with Mg<sub>3</sub>Bi<sub>2</sub> for enhanced thermoelectric performance. Materials Horizons. Published online November 20, 2017. https://doi.org/10.1039/C7MH00865A.